Characterization of unsteadiness in an overexpanded planar nozzle

Characterization of Unsteadiness in an Overexpanded Planar Nozzle

E. Martelli*
University of Campania Luigi Vanvitelli, 81031 Aversa, Italy
and
P. P. Ciottoli,† L. Saccoccio,‡ F. Nasuti,§ M. Valorani,¶ and M. Bernardini**
Sapienza University of Rome, 00184 Rome, Italy

DOI: 10.2514/1.J057162

The sea-level startup of rocket engines is characterized by the nozzle experiencing a high degree of overexpansion and consequent internal flow separation with a strong unsteady shock-wave/boundary-layer interaction. In this work, a three-dimensional planar overexpanded nozzle, characterized by an internal flow separation, has been simulated by means of the delayed detached-eddy simulation (DDES) method. The unsteady pressure signals have been analyzed by the wavelet decomposition to characterize their spectral content. The results indicate that the DDES approach is able to capture the shock oscillations, and the computed characteristic frequency is close to the ones available from literature for the same test case. The fundamental frequency computed in this work is lower than the one predicted by the model of the longitudinal acoustic frequency. The self-sustained oscillation is driven by a pressure imbalance between the pressure level downstream of the recompression shock and the ambient. Different nozzle pressure ratios (NPRs) have been simulated, all showing the same qualitative behavior, even if the test case with the highest NPR seems to be heavily influenced by the presence of a large region with reversed flow.

Nomenclature

a_0	=	speed of sound at chamber conditions
f	=	frequency
H_t	=	nozzle throat height
L_z	=	spatial extent of the computational domain
M	=	Mach number
Pr	=	molecular Prandtl number
Pr_t	=	turbulent Prandtl number
p_a	=	ambient pressure
p_w	=	wall pressure
p_0	=	chamber pressure
q_j	=	heat flux vector
Re	=	Reynolds number
S_{ij}	=	strain-rate tensor
St	=	Strouhal number
U_p	=	quasi-one-dimensional isentropic nozzle exit velocity
$W_n(s)$	=	wavelet coefficient
x	=	streamwise distance measured from nozzle throat
γ	=	specific heat ratio
Δ	=	subgrid length scale
ν_t	=	eddy viscosity
$\tilde{\nu}$	=	Spalart–Allmaras pseudo eddy viscosity
σ_w	=	standard deviation of wall pressure fluctuations

Subscripts

n	=	time index
s	=	wavelet scale

I. Introduction

SUPERSONIC rocket nozzles are characterized by a transient phase at startup, during which the flow is largely overexpanded, an internal recompression shock forms, and boundary-layer separation occurs. The consequent shock-wave turbulent boundary-layer interaction (SWBLI) causes the shedding of vortical structures and the unsteadiness in the shock-wave position. In such a situation dynamic side loads are produced, which can even lead to the failure of the nozzle structure [1]. Hadjadj and Onofri [2] and Reijasse et al. [3] collect various studies on the side-load generation and flow separation configurations. The main topic of this work is to increase the physical understanding of the low-frequency unsteadiness of a shock interacting with a turbulent pulsating separated flow, which is one of several research directions recommended by Hadjadj and Onofri [2]. In this study, attention is focused on a three-dimensional planar configuration; therefore, the following literature review is concentrated on previous investigations on this kind of geometry. Bogar et al. [4] investigated the unsteady flow characteristics of an overexpanded transonic diffuser. They observed that, in the case of attached flow (or very mild separation), the characteristic frequencies have an acoustic nature and scale with the distance of the shock from the diffuser exit, whereas in the case of separated flows, the characteristic frequencies scale with the length of the inviscid core flow. An experimental analysis of unsteady separated flows in a supersonic planar nozzle was carried out by Burgoing and Reijasse [5], who revealed that the low-frequency motion of the shock is governed by large structure dynamics in the separated flow regions. Handa et al. [6] indicated two possible mechanisms for the shock oscillation. In one case, pressure disturbances, generated in the downstream turbulent separated region, force the shock to oscillate, resulting in a broad shape of the power spectral density. The other case foresees the reflection of a disturbance at the diffuser exit (acoustic feedback), resulting in a narrow-shaped power spectral density. Papamoschou and Zill [7] and Johnson and Papamoschou [8] have studied the unsteady shock behavior in an overexpanded planar nozzle. Their results indicate a low-frequency pistonlike shock motion without any resonant tones. More recently, a similar

Received 6 February 2018; revision received 14 June 2018; accepted for publication 11 August 2018; published online Open Access 23 November 2018.

*Associate Professor, Department of Engineering, via Roma 29.
†Research Fellow, Department of Mechanical and Aerospace Engineering, via Eudossiana 18.
‡Ph.D. Student, Department of Mechanical and Aerospace Engineering, via Eudossiana 18.
§Associate Professor, Department of Mechanical and Aerospace Engineering, via Eudossiana 18. Associate Fellow AIAA.
¶Full Professor, Department of Mechanical and Aerospace Engineering, via Eudossiana 18.
**Assistant Professor, Department of Mechanical and Aerospace Engineering, via Eudossiana 18.

geometric configuration was studied by Verma et al. [9]. They found that, for low nozzle pressure ratios, the flow is characterized by a laminar SWBLI, and a resonant tone is present. At higher nozzle pressure ratios, the boundary layer becomes turbulent, the tone disappears, and the shock excursion length decreases.

As far as large/detached-eddy simulations (LES/DES) of SWBLI are concerned, not many papers can be found thus far. Among these, Garnier and Sagaut [10] carried out a large-eddy simulation of an oblique shock wave impinging upon a turbulent boundary at Mach number $M = 2.3$. They found generally good agreement between the computed mean global quantities and the experimental results. However, their simulation was not able to capture completely the low-frequency motion of the shock because of the difficulties in simulating a long physical time. The LES conducted by Touber and Sandham [11] provided an interesting insight regarding the low-frequency unsteadiness; the data were used to develop an analytical model [12] based on a stochastic ordinary differential equation, derived from the Navier–Stokes equations. This model describes the coupled shock/boundary-layer system as a first-order low-pass filter. Also, Hadjadj [13] and Aubard et al. [14] carried out a large-eddy simulation of a shock wave impinging on a turbulent boundary layer. The results revealed that the low frequencies of the shock/separation region coupled system are present also without an upstream low-frequency forcing. It seems therefore that they are not linked to a low-pass filtering effect, but they are a consequence of a global instability of the whole system.

Very few studies can be found in literature on the SWBLI in overexpanded nozzles. Deck [15] carried out a delayed detached-eddy simulation (DDES) of the end-effect regime in an axisymmetric overexpanded rocket nozzle flow characterized by a restricted shock separation. Although the experimentally measured main properties of the flow motion were rather well reproduced, the computed main frequency resulted to be higher than in the experiment. Olson and Lele [16] performed large-eddy simulations, at reduced Reynolds number, of the experiments of Johnson and Papamoschou, finding a certain level of agreement between the experimental data and the computed frequency of the shock displacement. The origin of the unsteadiness was attributed to the confinement of the exit area by the separated flow.

The use of a detached-eddy simulation [17], a hybrid Reynolds-averaged Navier–Stokes (RANS)/LES method, allows to simulate the flows typically present in subscale cold-gas supersonic nozzles [15,18], which are characterized by a Reynolds number of the order of 1 million and are still hardly predictable by means of large-eddy simulation technique. In this work, the three-dimensional (3-D) planar nozzle described in the experiments of Johnson and Papamoschou [8] and simulated with the LES technique by Olson and Lele [16] has been reproduced by means of the delayed DES (DDES) technique [19]. The term delayed indicates a method to prevent a too-early transition from RANS to LES inside the attached boundary layer. The first main target is the comparison between computational and experimental data regarding the unsteady flow behavior, to assess whether the DDES technique is able to describe this kind of flow. In particular, the shock excursion length and the characteristic Strouhal numbers of the unsteady wall pressure field have been determined and compared with the available data. A physical analysis has been attempted with the specific aim of identifying the driving mechanism of the shock unsteadiness. Then, a parametric study has been conducted to analyze the effect of the nozzle pressure ratio, or equivalently of the shock strength, on this unsteadiness.

The analysis of the dynamic pressure signals has been conducted by means of the wavelet technique. The wavelet transform is an analysis tool well suited to the study of multiscale, nonstationary processes occurring over finite temporal domains [20]. In particular, it is able to detect the localized variations of power within a time series. In fact, by decomposing a time series into time-frequency space, one is able to determine both the dominant modes of variability and how these modes vary in time.

The paper is organized as follows. In Sec. II, the numerical method is described, and the use of DDES is discussed in the frame of overexpanded nozzles. Section III presents the physical parameters of the test case and the numerical setup. Section IV presents the flowfield characteristics as well as the statistical and the spectral properties of the wall pressure unsteady signals. The parametric analysis at different NPR values is reported in Sec. V. Finally, in Sec. VI, the major findings of this investigation are reported.

II. Computational Setup

Hybrid RANS/LES modeling approaches have been proposed to simulate massively separated flows, such as the well-known DES [21]. A general feature of this approach is that the whole attached boundary layer is treated resorting to RANS, whereas LES is applied only in the separated flow regions.

A. Physical Model

The three-dimensional Navier–Stokes equations for a compressible, viscous, heat-conducting gas, which are adopted in this study, can be written as follows:

$$\frac{\partial \rho}{\partial t} + \frac{\partial(\rho u_j)}{\partial x_j} = 0,$$
$$\frac{\partial(\rho u_i)}{\partial t} + \frac{\partial(\rho u_i u_j)}{\partial x_j} + \frac{\partial p}{\partial x_i} - \frac{\partial \tau_{ij}}{\partial x_j} = 0,$$
$$\frac{\partial(\rho E)}{\partial t} + \frac{\partial(\rho E u_j + p u_j)}{\partial x_j} - \frac{\partial(\tau_{ij} u_i - q_j)}{\partial x_j} = 0 \tag{1}$$

where ρ is the density, u_i is the velocity component in the ith coordinate direction ($i = 1, 2, 3$), E is the total energy per unit mass, and p is the thermodynamic pressure. The total stress tensor τ_{ij} is the sum of the viscous and the Reynolds stress tensor:

$$\tau_{ij} = 2\rho(\nu + \nu_t) S^*_{ij} \qquad S^*_{ij} = S_{ij} - \frac{1}{3} S_{kk} \delta_{ij} \tag{2}$$

where the Boussinesq hypothesis is applied through the introduction of the eddy viscosity ν_t; $S_{ij} = (u_{i,j} + u_{j,i})/2$ is the strain-rate tensor; and ν is the kinematic viscosity, depending on the temperature T through Sutherland's law. Similarly, the total heat flux q_j is the sum of a molecular and a turbulent contribution:

$$q_j = -\rho c_p \left(\frac{\nu}{Pr} + \frac{\nu_t}{Pr_t} \right) \frac{\partial T}{\partial x_j} \tag{3}$$

where Pr and Pr_t are the molecular and turbulent Prandtl numbers, assumed to be 0.72 and 0.9, respectively. Hybrid RANS/LES capabilities are provided through the implementation of the delayed detached-eddy simulation (DDES) approach based on the Spalart–Allmaras model [22], which involves a transport equation for a pseudo eddy viscosity $\tilde{\nu}$:

$$\frac{\partial(\rho\tilde{\nu})}{\partial t} + \frac{\partial(\rho\tilde{\nu} u_j)}{\partial x_j} = c_{b1}\tilde{S}\rho\tilde{\nu} + \frac{1}{\sigma}\left[\frac{\partial}{\partial x_j}\left[(\rho\nu + \rho\tilde{\nu}) \frac{\partial \tilde{\nu}}{\partial x_j} \right] + c_{b2}\rho \left(\frac{\partial \tilde{\nu}}{\partial x_j} \right)^2 \right] - c_{w1} f_w \rho \left(\frac{\tilde{\nu}}{\tilde{d}} \right)^2 \tag{4}$$

where $\tilde{d}$ is the model length scale, f_w is a near-wall damping function, $\tilde{S}$ is a modified vorticity magnitude, and $\sigma, c_{b1}, c_{b2}, c_{w1}$ are model constants. The eddy viscosity in Eq. (2) is related to $\tilde{\nu}$ through $\nu_t = \tilde{\nu} f_{v1}$, where f_{v1} is a correction function designed to guarantee the correct boundary-layer behavior in the near-wall region. In DDES, the destruction term in Eq. (4) is designed so that the model reduces to pure RANS in attached boundary layers and to a LES subgrid-scale one in the detached flow regions. This is accomplished by defining the length scale $\tilde{d}$ as

$$\tilde{d} = d_w - f_d \max(0, d_w - C_{\mathrm{DES}}\Delta) \tag{5}$$

where d_w is the distance from the closest wall, and Δ is the subgrid length-scale, controlling the wavelengths resolved in LES mode.

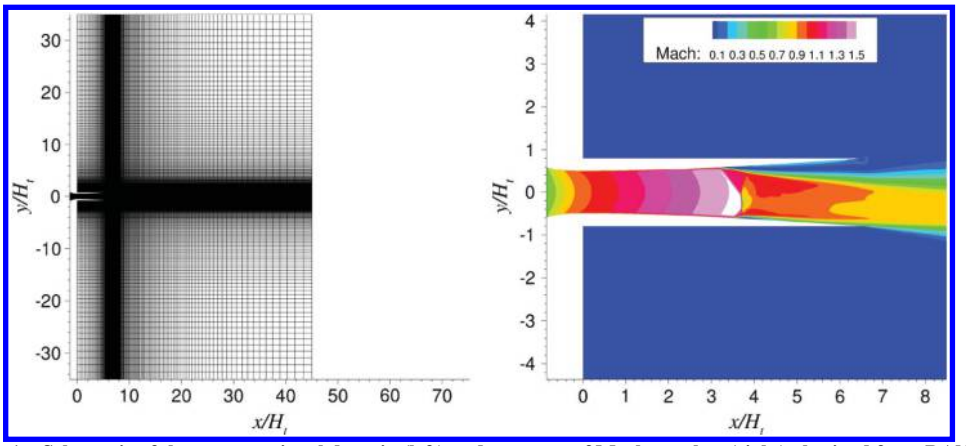

Fig. 1 Schematic of the computational domain (left) and contours of Mach number (right) obtained from RANS.

C_{DES} is a calibration constant equal to 0.20. The function f_d, designed to be 0 in boundary layers and 1 in LES regions, reads as

$$f_d = 1 - \tanh\left[(8r_d)^3\right], \qquad r_d = \frac{\tilde{\nu}}{k^2 d_w^2 \sqrt{U_{i,j}U_{i,j}}} \tag{6}$$

where $U_{i,j}$ is the velocity gradient, and k is the von Kármán constant. The introduction of f_d distinguishes DDES from the original DES approach [17] (usually denoted as DES97), ensuring that boundary layers are treated in RANS mode also in the presence of "ambiguous" grids in the sense defined by Spalart et al. [22], for which the wall-parallel spacings do not exceed the boundary-layer thickness. The DDES strategy prevents the phenomenon of model stress depletion, consisting of the excessive reduction of the eddy viscosity in the region of switch (grey area) between RANS and LES, which in turn leads to grid-induced separation.

Differently from the original DDES formulation and following Deck [23], the subgrid length scale in this work is not only defined as the largest spacing in all coordinate directions $\Delta_{\max} = \max(\Delta x, \Delta y, \Delta z)$, but it depends on the flow itself, through f_d, as follows:

$$\Delta = \frac{1}{2}\left[\left(1 + \frac{f_d - f_{d0}}{|f_d - f_{d0}|}\right)\Delta_{\max} + \left(1 - \frac{f_d - f_{d0}}{|f_d - f_{d0}|}\right)\Delta_{\mathrm{vol}}\right] \tag{7}$$

where $f_{d0} = 0.8$, and $\Delta_{\mathrm{vol}} = (\Delta x \cdot \Delta y \cdot \Delta z)^{1/3}$. This definition guarantees that the attached boundary layers are treated in RANS mode, even in the case of very refined grids and accelerates the transition from RANS to LES. Because of the high level of stretching in the mesh, $\Delta = \Delta_{\mathrm{Vol}}$ results to be lower than $\Delta_{\max}$; the destruction term is enhanced, and this helps to unlock the Kelvin–Helmholtz instability in the separated shear layer.

B. Numerical Method

Numerical simulations are carried out by means of an in-house, fully validated compressible flow solver [18,24] that exploits a centered second-order finite volume approach and takes advantage of an energy consistent formulation (away from shocks). Cell-face values of the flow variables are taken as the average of the two cell values on either side of that face, as in Jameson [25]. In smooth flow regions, the adopted reconstruction is able to guarantee that the overall kinetic energy of the fluid is preserved, in the limit of inviscid, incompressible flow [26]. This property is particularly beneficial for flow regions treated in LES mode, where the grid is sufficiently fine to support the development of LES content and where the only relevant dissipation (in addition to the molecular one) should be that provided by the turbulence model. The discretization scheme is made to switch to third-order weighted essentially nonoscillatory near discontinuities, identified by a modified Ducros sensor [27]:

$$\Theta = \frac{(\nabla \cdot u)^2}{(\nabla \cdot u)^2 + (\nabla \times u)^2 + \epsilon} \tag{8}$$

where the small positive number ϵ of the original formulation is here set as $\epsilon = a_0/H_t$ to reduce the sensitivity to dilatational fluctuations and guarantee that the sensor is only activated when the local dilatation becomes larger than a typical large-scale velocity gradient [26]. The gradients normal to the cell faces needed for the viscous fluxes are evaluated through second-order central-difference approximations, obtaining compact stencils and avoiding numerical odd–even decoupling phenomena. Time advancement of the semidiscretized system of ODEs resulting from the spatial discretization is carried out by means of a low-storage third-order Runge–Kutta algorithm [28]. The code is written in Fortran 90, uses domain decomposition, and fully exploits the message passing interface paradigm for the parallelism.

III. Test Case Description

The nozzle geometry has been taken from case 3 of the work of Johnson and Papamoschou [8]. The throat height is equal to 17.8 mm, the nozzle length (from the throat) is 117 mm, the width is 63.5 mm, and the area ratio A_e/A_t is 1.6. A two-dimensional schematic of the computational domain adopted for the simulation is presented in Fig. 1a. It includes the nozzle with the external ambient, and the zero of the x axis is located at the nozzle throat. A Cartesian structured mesh is generated using the conformal mapping algorithm of Driscoll and Vavasis [29] and the open-source tool gridgen-c.[††] The computational mesh inside the nozzle consists of $N_x \cdot N_y \cdot N_z = 512 \cdot 256 \cdot 96$ cells for a total number of $N_{xyz} \approx 12.6 \cdot 10^6$ cells. The grid density of this test case is very similar to the mesh "B" of Olson and Lele [16], whose LES will be considered for the rest of this paper as the reference LES for the present DDES case. Note that, different from the reference LES, the flow in our simulation develops from stagnation conditions, and the convergent part of the nozzle is included in the computation. The whole external domain has the same number of cells of the nozzle; therefore, the total number of volumes is approximately equal to 25 million. The boundary conditions have been imposed according to the following scheme. At the inlet station in the nozzle, a subsonic flow is prescribed by imposing the total pressure, total temperature, and the flow direction; the top and bottom boundaries are treated as adiabatic no-slip walls; at the right section of the external domain an outflow condition is imposed by means of an extrapolation of the integration variables to avoid any longitudinal acoustic coupling; and characteristics-based boundary conditions prescribing the backpressure are assigned on all the other external boundaries. A coflow velocity was not imposed in the external environment. In the spanwise direction, we follow the reference LES [30] by selecting a spanwise width of the computational domain $L_z/H_t = 0.9$ and applying periodic boundary conditions. The 3-D DDES initial condition is obtained from an extrusion in the spanwise

[††]Data available online at https://github.com/sakov/gridgen-c [retrieved 14 May 2018].

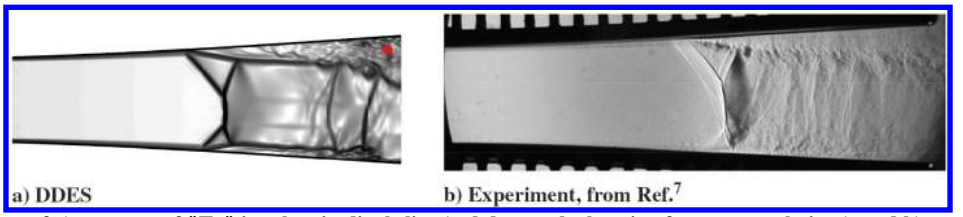

Fig. 2 Representations of a) contours of $\|\nabla\rho\|$ in a longitudinal slice (red dot: probe location for autocorrelations), and b) spark schlieren image of supersonic nozzle flow separation.

direction of the two-dimensional steady-state RANS solution. To promote the development of turbulent structures, a sinusoidal perturbation with maximum magnitude of 0.5% has been superimposed on the mean density field at the initial time of DDES in a limited region in space between $x = 3.5H_t$ and $x = 6H_t$. The simulations were performed on the supercomputers Galileo (IBM NextScale) and Marconi (Lenovo NeXtScale Platform) of the Italian Computing Center CINECA. The computational time step is equal to $1.3 \cdot 10^{-5}$ s, and the simulation ran approximately for 0.04 s, after an initial transient period of 0.02 s (approximately 10 low-frequency cycles of the shock motion) that was discarded. The maximum Courant–Friedrichs–Lewy number is 0.2.

The present internal flowfield is characterized by the nozzle pressure ratio NPR $= p_0/p_a$, where p_0 and p_a denote the chamber and ambient pressure respectively. In this work, the NPR selected is 1.7 ($p_0 = 1.7$ bar), equal to the case 3 of the study of Olson and Lele [16]. The nozzle Reynolds number is based on the chamber values and the throat half-height:

$$Re = \frac{\sqrt{\gamma}}{\mu}\frac{p_0 H_t/2}{\sqrt{R_{\text{air}}T_0}} = 3.3 \cdot 10^5$$

where γ is the constant specific heat ratio, μ is the molecular viscosity evaluated at the chamber temperature $T_0 = 300$ K, and R_{air} is the air gas constant. It is important to note that the Reynolds number of the reference LES case was reduced to $8.9 \cdot 10^4$ for computational reasons [16]. Figure 1b shows the Mach number flowfield; it can be seen that the shock has the classical λ shape and that the flow separation is not symmetric: on one side is large and open to the external ambient, whereas on the other is small and closed. This asymmetry is confirmed by the experiments [7]; Fig. 2a shows an instantaneous snapshot of the magnitude of the density gradient, which is compared with an image of the spark schlieren of the experiment. It can be seen that the separation-shock structure and the extension of the separated regions are qualitatively well reproduced. A similar nonsymmetric shock structure can be found in Verma et al. [9].

IV. Results

A. Instantaneous Flowfield

The main characteristics of the instantaneous flowfield are shown in Fig. 3a. The 3-D turbulent structures are represented by showing a positive isovalue of the second invariant of the anisotropic part of the deformation rate tensor ($\boldsymbol{A}^* = \boldsymbol{A} - \theta/3\boldsymbol{I}$), where θ is the flow dilatation. Such definition represents an extension of the Q-criterion to compressible flows [31] and allows to identify tubelike vortical structures. The isosurface is colored by the local value of the streamwise velocity. The slice in the last Z plane shows the field of the magnitude of the density gradient, useful to individuate the shocks and the shear layers. Looking at the top wall (note that the y axis has changed orientation to better illustrate the flow features), which develops the most important separated region, it is possible to notice at first the formation of almost two-dimensional vortical structures in the shear layer, which are then replaced by three-dimensional structures developing downstream. It can be seen therefore that there is still an important region that remains in the so-called gray area; in this zone, the flow is not treated in RANS mode nor in LES mode. The bottom wall, characterized by a very small separation, remains almost in RANS mode and develops a turbulent content just at the nozzle exit. Figure 3b shows an instantaneous field of the longitudinal component of the nondimensional vorticity on the top wall, which

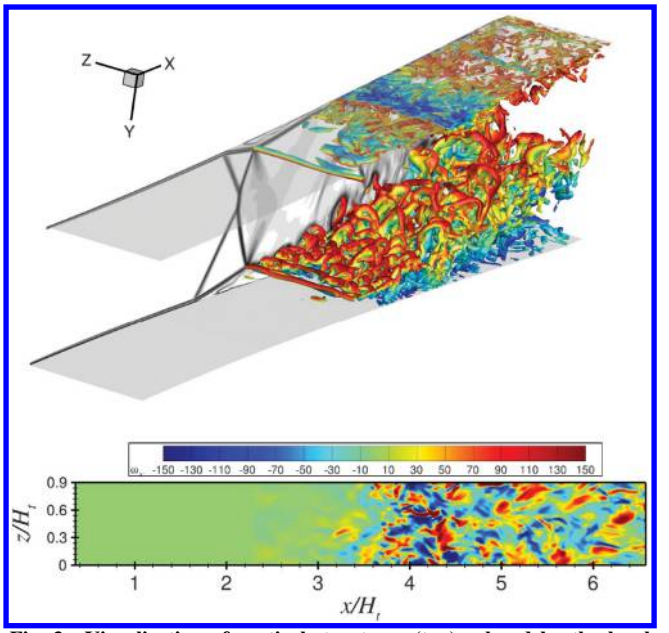

Fig. 3 Visualization of vortical structures (top) colored by the local streamwise velocity and contours of streamwise vorticity on the top wall (bottom).

qualitatively indicates the three-dimensionality of the field in the spanwise direction and the growth of the turbulent structures in the longitudinal direction. At this point, it is important to assess whether the extension of the domain in z is sufficient to avoid confinements effects on the large-scale turbulent structures. To evaluate this, the two-point correlation of the fluctuations in the spanwise direction has been computed in the turbulent region according to

$$R_{\phi'}(r_z) = \frac{\overline{\phi'(x,y,z,t)\phi'(x,y,z+r_z,t)}}{\sigma_\phi^2(x,y)} \tag{9}$$

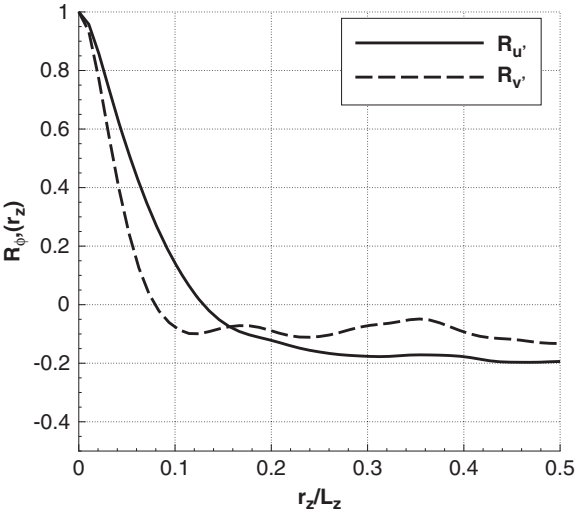

Fig. 4 Two point autocorrelation for longitudinal and vertical velocity fluctuations in the spanwise direction.

where ϕ' represents the fluctuations of the longitudinal velocity or of the vertical velocity component and σ is the standard deviation. The results are reported in Fig. 4b for a representative probe location (shown in Fig. 2a), with the others being qualitatively similar. We observe that the correlation substantially decays for $r_z/L_z < 0.2$, although a certain degree of anticorrelation persists, in line with the findings of Olson and Lele [30]. This result was judged as a satisfactory compromise between accuracy and computational cost.

A significant self-sustained shock oscillation characterizes the flowfield. Figure 5 shows the field of the density gradient magnitude on the left together with distribution of the static pressure in the nozzle symmetry plane at the centerline on the right. The red color represents downstream movement of the flow separation, whereas the blue color represents upstream movement. The black dashed line indicates the value of the nondimensional ambient pressure p_a/p_0. The nondimensional time is indicated as $t^* = tU_p/H_t$, where t is

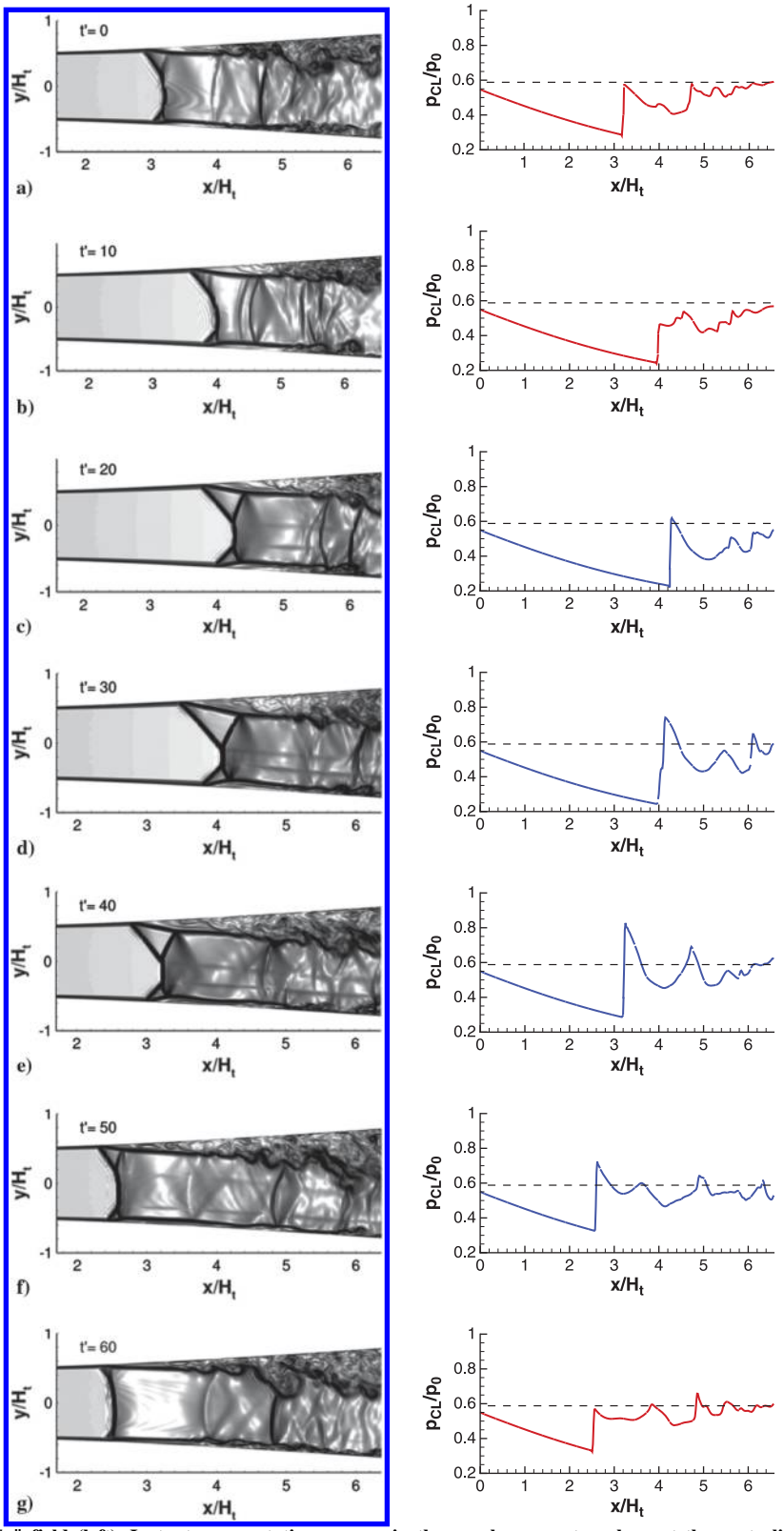

Fig. 5 Snapshots of the $\|\nabla\rho\|$ field (left). Instantaneous static pressure in the nozzle symmetry plane at the centerline (right). Red: downstream movement; blue: upstream movement; black dashed line: p_a/p_0.

time, and U_p is the quasi-one-dimensional velocity at the nozzle exit, computed by the isentropic relations. The sequence begins at $t^* = 0$ (the zero value is arbitrary chosen) with the downstream movement of the shock system, characterized by a pressure immediately behind the shock that becomes lower and lower than the ambient value (at $t^* = 0$ and $t^* = 10$). This difference is due to the low shock Mach number at the beginning of the downstream movement and by the movement itself. When the shock reaches its extreme downstream positions, the shock train increases its intensity, and the pressure value behind the shock becomes higher than the ambient pressure ($t^* = 20$). At this point, the shock begins to move upstream. Now, the sequence of this movement is characterized always by a pressure behind the shock higher than the ambient value. At $t^* = 50$, the shock slows down because the shock Mach number is now decreasing due to the lower area ratios, and the pressure behind the shock at first approaches the ambient value and then becomes lower ($t^* = 60$). At this point, the downstream movement starts again, completing the cycle. It can be seen that the shock excursion is large, more than one throat height, and the shock configuration changes in shape and intensity. At $t^* = 20$, the shock is near the nozzle exit, the shock Mach number is equal to 1.61, and there are important separated regions over both the walls. The interaction of the reflected shocks with the shear layers are well visible, together with the expansion fans, which accelerate the flow to a supersonic Mach number and decrease the local static pressure well below the ambient pressure. A second shock then appears to slow down the flow to subsonic velocity. At $t^* = 60$, the separation is nearly at its upstream position. The shock Mach number is equal to 1.36, the λ shocks are smaller, and consequently the zones characterized by a reverse flow are less pronounced.

This oscillating behavior of the static pressure behind the shock system is reflected in the wall pressure behavior. Figure 6a shows again a cycle as seen by the top wall; in this case, the incipient separation points of the shock during the upstream and downstream movement are taken at the same location for direct comparison. The difference in the values of the plateau pressure p_p, that is the pressure at the beginning of the plateau region downstream of the shock as defined in Östlund [32], is evident. During the upstream movement, the plateau pressure is higher than the corresponding value of the downstream movement. A local nozzle pressure ratio can be defined using p_p instead of p_a, $\mathrm{NPR}_p = p_0/p_p$. In a previous work of the authors [33], it has been shown that it is this local NPR_P that governs the position of the separation line. Figure 6 reports the NPR_P's during an instantaneous cycle, and a hysteresis phenomenon is evident. The following steps can be identified.

1) At the beginning of the downstream movement, the shock Mach number M_s is low due to the local area ratio and due to the movement itself. The plateau pressure is low, the NPR_P increases and the separation line is pushed forward.

2) When the shock system reaches its extreme positions, the increase of the area ratio increases M_s and consequently the value of p_p; as a consequence, NPR_P starts decreasing, and the extension of the reverse flow becomes more and more important. This causes the slowdown of the shock at first and then the change of direction.

3) At the beginning of the upstream movement, M_s is high due to local area ratio and due to the movement itself. The value of the NPR_P decreases.

4) Finally, when the extreme upstream position is reached, the shock Mach number decreases due to the lower area ratio, the extension of the reverse flow is heavily reduced, the plateau pressure decreases, and NPR_P increases. Again, there is a process of deceleration and change of direction, completing the cycle.

These features are typical of shock train configurations, which are characterized by a self-sustained oscillation, as reported in the review of Matsuo et al. [34] and references therein. In a very recent experimental work [35], Xiong et al. investigated the response of a shock train in a straight channel to downstream excitations. They found that the shock system undergoes a periodical oscillation in response to the external forcing. Moreover, different from the cases with steady backpressure, the mechanism by which the shock train adapts to downstream excitations is to keep on moving so that the relative Mach number ahead of the shock train changes to match the varying imposed backpressure. The shock dynamics described in the present DDES simulation is qualitatively very similar to the experimental findings of Xiong et al. [35]; therefore, it could be argued that the subsonic turbulent recirculating region acts as an external source of unsteady pressure forcing, causing the periodic motion of the shock system.

B. Wall Pressure Signature

The statistical properties of the fluctuating pressure are first analyzed by evaluating the averaged properties together with the variance of the pressure fluctuations and comparing them with the available experimental data. Figure 7a shows the streamwise distribution of the numerical and experimental time and spanwise-averaged top-wall pressure, made nondimensional by the ambient pressure p_a. It can be seen that the RANS solution predicts well the position of the mean separation point but overpredicts the pressure level in the recirculating region. Instead, the DDES solution predicts very well the static pressure in the separated zone, although separation is anticipated with respect to the experiment, as a consequence of a greater shock excursion length that spreads the wall pressure over a longer streamwise distance. Figure 7b shows the nondimensional variance of the wall pressure fluctuations, together with the experimental values. Within the attached boundary layer, σ_w is zero because, according to the DDES approach, this flowfield region is automatically treated in RANS mode. Instead, downstream of the separation point, there is a peak in the standard deviation value, corresponding to the excursion zone of the shock

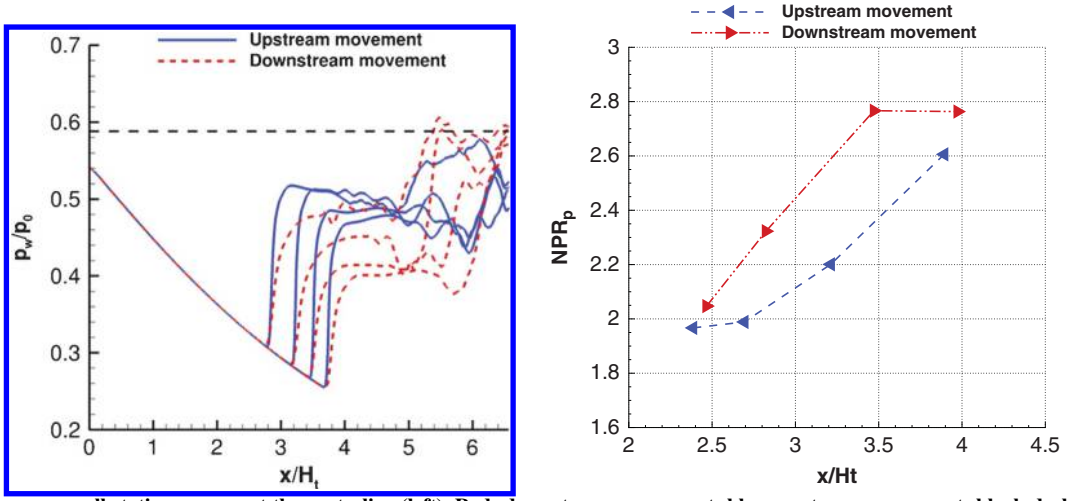

Fig. 6 Instantaneous wall static pressure at the centerline (left). Red: downstream movement; blue: upstream movement; black dashed line: p_a/p_0. Hysteresis cycle of the local nozzle pressure ratio $\mathrm{NPR}_p = p_0/p_p$ (right).

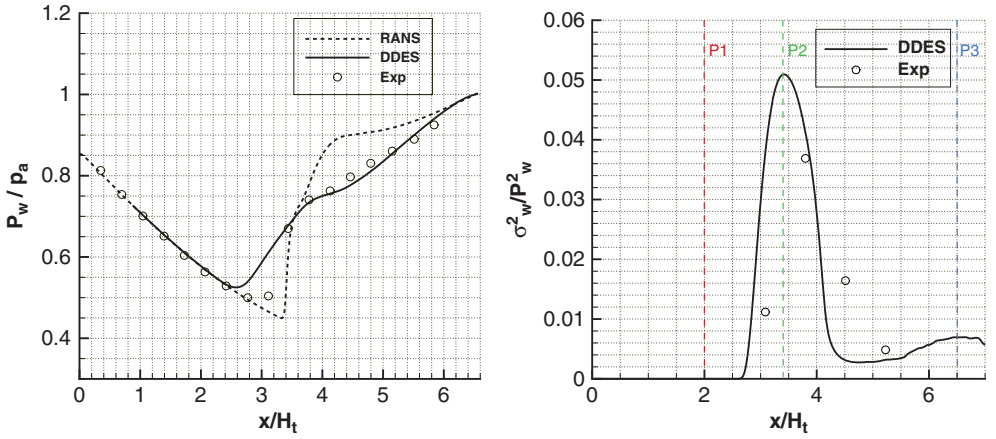

Fig. 7 Streamwise distribution of mean top-wall pressure (left) and pressure fluctuations variance (right).

system. Moving downstream, the first part of the separated region is characterized by a decrease of σ_w, whereas a second increase is observable downstream, associated to the developing turbulent shear layer in the last part of the nozzle. The numerical trend is very similar to the experimental one. The numerical maximum value of the variance is higher than the experimental value, again due to a more important shock excursion length. It can be noted that the distribution of the wall pressure fluctuations is qualitatively very similar to the distributions found in other classical shock-wave/boundary-layer interaction; see for example the experimental findings of Dupont on an incident shock on a flat plate [36,37] and of Dolling on a supersonic flow over a compression ramp [38]. In Fig. 7b, the position of three numerical pressure probes is also reported. P_1 is located in the attached (RANS) region, P_2 is located where the wall pressure fluctuation standard deviation has the maximum value corresponding to the shock oscillation, and P_3 is positioned in the turbulent recirculation region near the nozzle exit. Figure 8a shows a set of instantaneous, spanwise-averaged wall pressure distributions and illustrates the entity of the shock excursion. The position of the separation point can be qualitatively indicated by the minimum value reached by the wall pressure. It can be seen that the separation excursion has a significant variation with time. Figure 8b shows a temporal slot of the wall pressure signals from probes P_1, P_2, and P_3. It can be seen that the first signal is characterized by no oscillations. The second one is characterized by the passage of the foot of the separation shock. When the shock is downstream of the probe P_2, the wall pressure value is related to the attached supersonic flow, whereas when the shock is upstream of the probe, the wall pressure value is related to the recirculating subsonic region. The probe P_3 is most of the time downstream of the shock; therefore, the signal is typical of a turbulent separated region. The downward spikes in the pressure behavior indicate the important influence of the shock movement in this downstream region.

C. Wavelet Spectral Analysis

The continuous wavelet transform is applied to the unsteady wall pressure signals to decompose them in the time-frequency space. An extended review of the application of wavelets to study turbulence phenomena can be found in Farge [39], whereas only the key theoretical aspects are here reported. The continuous wavelet transform of a discrete time sequence p_n, with equal spacing δt and $n = 0, \ldots, N-1$, is defined as the convolution of p_n with a scaled and translated version of the mother wavelet ψ_0:

$$W_n(s) = \sum_{n'=0}^{N-1} p_n \cdot \psi^* \left[\frac{(n'-n)\delta t}{s} \right] \tag{10}$$

where $*$ denotes the complex conjugate. By varying the wavelet scale s and translating along the time index n, one can construct a picture showing how the amplitude of the wavelet coefficients vary with the scale and with the time. In this study, the Morlet wavelet has been chosen because higher resolution in frequency can be achieved when compared with other mother functions. It consists of a plane wave modulated by a Gaussian:

$$\psi_0(\eta) = \pi^{-1/4} e^{i\omega_0 \eta} e^{-\eta^2/2} \tag{11}$$

where η is a nondimensional time parameter, and ω_0 is the nondimensional frequency, here taken equal to 6 to satisfy the

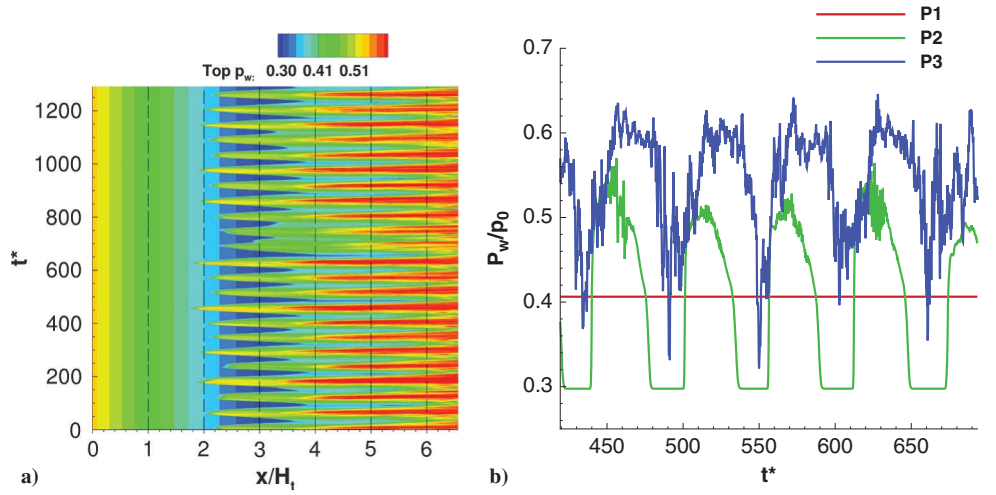

Fig. 8 Representations of a) streamwise distributions of instantaneous spanwise-averaged wall pressures, and b) temporal slot of the wall pressure signals from probes P_2 and P_3.

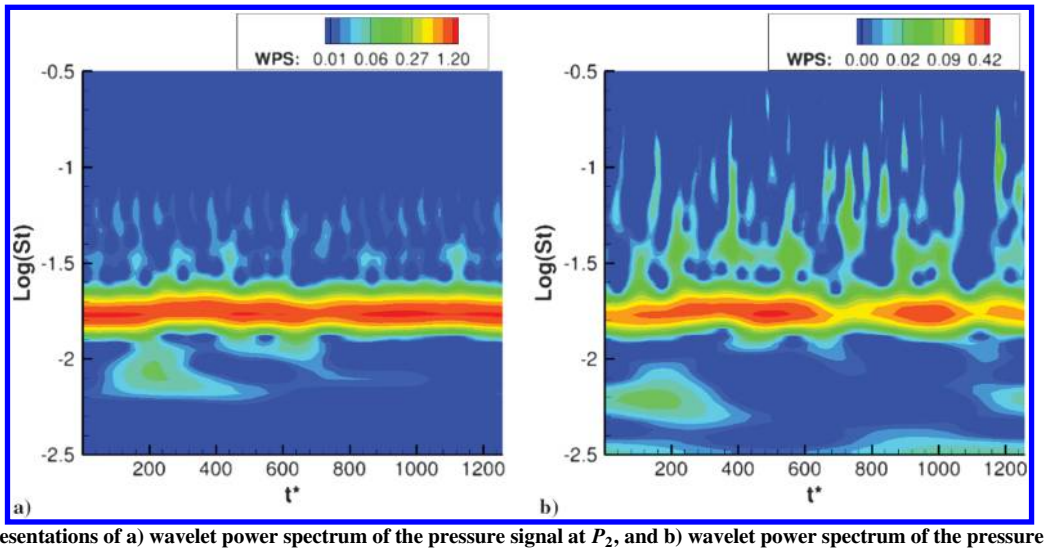

Fig. 9 Representations of a) wavelet power spectrum of the pressure signal at P_2, and b) wavelet power spectrum of the pressure signal at P_3.

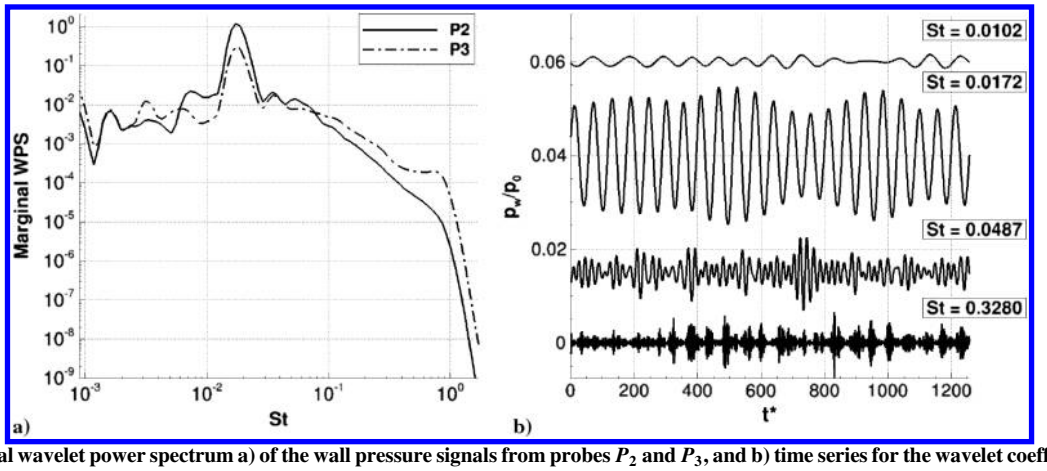

Fig. 10 Marginal wavelet power spectrum a) of the wall pressure signals from probes P_2 and P_3, and b) time series for the wavelet coefficients (probe 2) for different frequency modes.

admissibility condition [20]. The relationship between the equivalent Fourier period λ and the wavelet scale s can be found analytically [20]. For the Morlet wavelet with $\omega_0 = 6$, it is possible to find that $\lambda = 1.03$ s. From the definition of the wavelet coefficient, one can directly define the wavelet power spectrum (WPS) as $|W_n(s)|^2$. The WPS allows to build the wavelet scalogram, which provides a decomposition of the energy onto the scale-time (or frequency-time) plane. A Fourier-like spectrum can be simply recovered by a time averaging (marginal wavelet power spectrum).

Figure 9a shows the wavelet power spectrum of the wall pressure signal from probe P_2. The wavelet decomposition indicates that most of the energy is located in a nearly uniform way around a Strouhal number, defined as $St = fH_t/U_p$, where f is the frequency, equal to 0.017. The WPS of the signal from P_3 is reported in Fig. 9b. The effect of the shock motion on the spectrum is always present, with most of the energy concentrated around $St = 0.017$. In addition, the energy coming from the turbulent structures is also present at higher Strouhal number. The WPS is now characterized by an increased degree of intermittency: bursts of high energy are followed by region of low energy, and they are spread over a wider region of Strouhal number, between 0.03 and 0.1. The marginal WPSs of the two pressure signals are shown in Fig. 10a. This plot can give information similar to that given by the Fourier spectrum. Both the spectrum from P_2 and P_3 are characterized by the peak around $St = 0.017$, due to the shock movement. The signal from P_2 is characterized by a higher energy because it is located in the middle of the shock oscillation. The spectrum from P_3 shows a higher energy from Strouhal number greater than 0.08. This energy is characteristic of the fully turbulent subsonic recirculating region. Figure 10b shows the time series of a selection of the wavelet coefficients for different frequency modes. It must be noted that the various modes are shifted along the pressure axis to facilitate understanding. This picture shows the more relevant contribution, which corresponds to the peak shock Strouhal number of 0.017. This component is similar to a sinusoid with an amplitude modulation, whereas the components at higher frequencies are more typical of a turbulent flowfield.

Figure 11 shows the normalized autospectra of the shock position fluctuations for the present DDES simulation and for the reference LES. The shapes of the two spectra are very similar, and

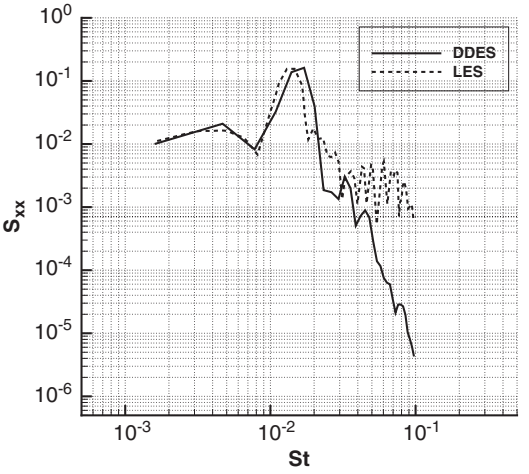

Fig. 11 Frequency spectrum of the shock position fluctuations.

Table 1 Comparison among DDES, LES [16], and experiment [8] of the shock Strouhal and shock excursion length

Shock property	DDES	LES	Experiment
Strouhal	0.0172	0.0122	$0.019 \leq St \leq 0.026$
Excursion	$1.52H_t$	$1.38H_t$	$0.9H_t$

there is a good agreement in the prediction of the peak Strouhal number corresponding to the shock motion. At higher frequencies, the DDES spectrum shows lower energy than LES, as a consequence of the fact that separation is partly governed by the RANS model. The values of the shock excursion length and of the peak shock Strouhal number are compared with the results of the experiment [8] and with the findings of the reference LES [16] in Table 1. It can be seen that the computed peak Strouhal number is very near to the range of the experimental values and close to the LES value. It is observed that the shock excursion length is very close to the reference LES value; however, both are higher than the experimental value. One of the main differences with the experiment is the absence of the lateral walls, which are substituted by the periodic conditions in the spanwise direction to save computational time. This aspect deserves more attention in future simulations.

D. Discussion on the Self-Sustained Oscillation

According to Zaman et al. [40] and Handa et al. [6] and references therein, there are two possible explanations for the unsteadiness. The first mechanism involves a longitudinal acoustic resonance, where the shock acts as an upstream closed end. The fundamental frequency corresponds to the case when one-quarter wavelength is fitted in the distance between the foot of the shock and the nozzle exit. The second explanation foresees a downstream propagating vorticity wave, which upon interaction with the nozzle exit produces a feedback acoustic wave traveling upstream. In the first case and following Morse [41], the fundamental frequency can be predicted by the expression:

$$f_m = \frac{a}{4l_p}\sqrt{m^2 + \frac{8l_p}{\pi^2 x_0}}, \qquad m = 1, 3, 5, \ldots$$

where a is the speed of sound in the separated region (approximately equals to 330 m/s), and

$$l_p = L + \frac{4D_e}{3\pi}, \qquad x_0 = \frac{D_t}{2\tan(\theta)}$$

Because a planar geometry has been used, it is necessary to compute an equivalent half-angle of divergence θ_e and the equivalent diameters ($D_{t,e}$ and $D_{e,e}$) according to following expressions [40]:

$$D_{t,e} = \sqrt{\frac{2}{\pi}(H_e + H_t) * H_t}$$

$$D_{e,e} = \sqrt{\frac{2}{\pi}(H_e + H_t) * H_e}$$

$$\theta_e = \tan^{-1}[(D_{e,e} - D_{t,e})/(2L)]$$

Using the data of this test case, the fundamental frequency ($m = 1$) corresponds to a Strouhal number of 0.026, higher than the value computed with the DDES method and with the LES method by Olson and Lele [16]. In addition, the experiment reveals a very broad spectrum, whereas the transonic resonance foresees a spectrum with a well-defined peak. Thus, it seems that the oscillation is not merely due to an acoustic resonance, if any. It must be considered that, in this case, there is an important interplay with the turbulent separated flowfield. In the test cases described by Zaman, the separation zone appears as a closed recirculation bubble, whereas in this case, the separation is open to the external ambient. Another difference with the experimental test cases of Zaman is the presence of a shock train in this planar nozzle. Therefore, these considerations on the acoustic resonance cannot directly be applied to the present flow configuration, where, as shown before, the shock oscillation is mainly associated to a pressure

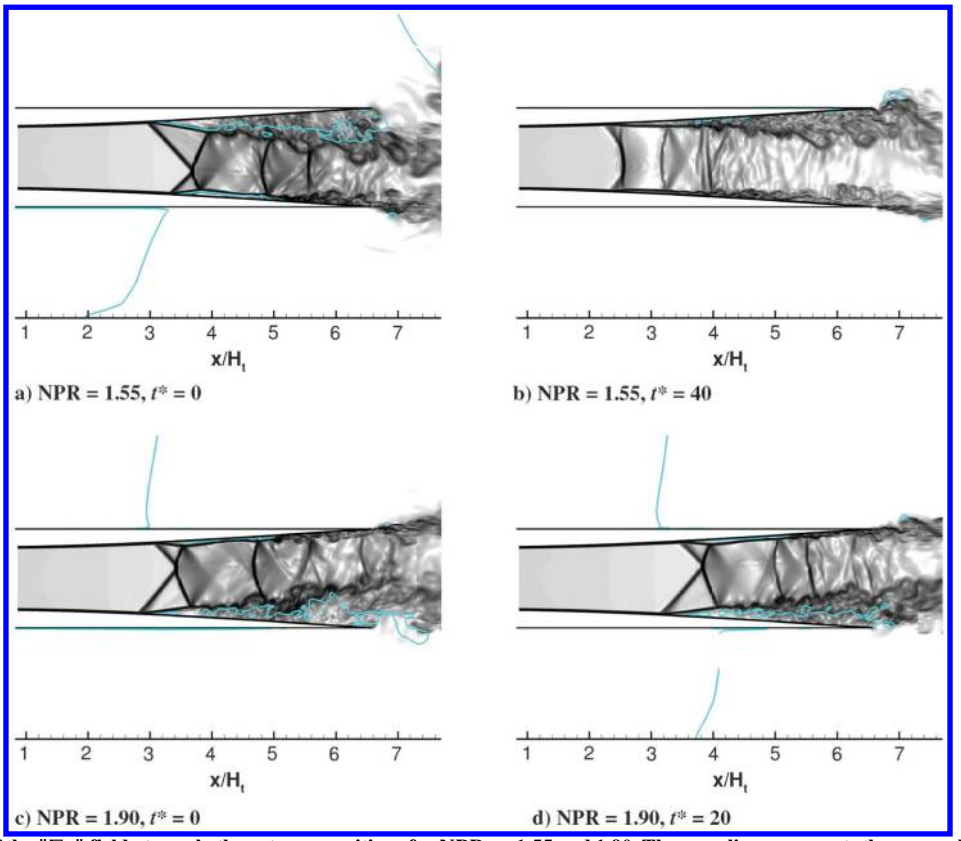

Fig. 12 Snapshots of the $\|\nabla\rho\|$ field at nearly the extreme positions for NPR = 1.55 and 1.90. The cyan line represents the zero value of the longitudinal velocity.

imbalance between the values behind the shock and the ambient. In fact, an equilibrium position is never found, and a limit cycle is established. Further investigations are necessary to understand which is the physical mechanism that feeds the instability and what kind of phenomenon imposes the characteristic time scale.

V. Parametric Analysis

After having assessed and analyzed the results of the reference test case at NPR = 1.70, two other NPRs (1.55 and 1.90) have been simulated to see the effect of the nozzle pressure ratio on the shock excursion L_s and on the spectral content of the pressure signals. These tests correspond to cases 1 and 5 of Olson and Lele [16], with the difference that, in the cited paper, the nozzle area ratio was varied to keep the shock at the same location (in average), whereas in the present tests, only the NPRs are varied. Figure 12 shows the snapshots of the magnitude of the density gradient field for NPR = 1.55 and 1.90, at the extreme position reached during half a cycle. It can be noted that, in the first case, the flow characteristics are almost equal to the case at NPR = 1.70; in particular, there is nearly no reverse flow when the shock is at its upstream position (Fig. 12b). The situation changes at NPR = 1.90. It can be seen that, in this case, a reverse flow is always present at the bottom wall. Consequently, the shock shape is unchanged between the two extreme positions (Figs. 12c and 12d).

Hysteresis cycles can also be found at these two other NPRs, whose extension can be appreciated in Fig. 13. At NPR = 1.70, there is the cycle with the greatest area, whereas at NPR = 1.90, there is instead an important area reduction. Figure 14 shows, for all the NPRs, the instantaneous, spanwise-averaged wall pressure distributions for all the simulation time. Qualitatively, the time histories are similar, but it is evident that the flow separation (and shock) range is reduced at NPR = 1.90. This can be quantified in Fig. 15, which shows the time average of the shock excursion length. A nonmonotonic behavior can be seen; L_s increases between NPR = 1.55 and NPR = 1.70, and then there is an important decrease at NPR = 1.90. At this pressure ratio, L_s is equal to 0.8 nozzle throat diameter, that is nearly half of the value of the excursion length for NPR = 1.7. Figure 15 shows also that the same nonmonotonic trend can be found for the peak value of the wall pressure fluctuations variance for the various NPRs; when the NPR changes from 1.55 to 1.70, there is an increase in the peak value, whereas when the NPR is further increased to 1.90, the peak shows an important decrease. It is not clear why there is this nonmonotonic behavior in the shock excursion and in the pressure oscillation level. It has been noted before that, at NPR = 1.55 and 1.70, the shock system oscillates between a configuration with a very small reverse flow region downstream of the shock and a configuration with an important region with reverse flow downstream of the shock. Instead, at NPR = 1.90, the shock oscillates between two configurations always characterized by an important reverse flow. This can be caused by the fact that, at this NPR, the shock Mach number is higher than at the two other configurations, inducing a higher degree of separation. And it can be argued that this regime is more dissipative, reducing the shock excursion length.

The wavelet power spectra have been computed for these two other NPRs and compared with the reference test case at NPR = 1.70. Again, the unsteady pressure signals from numerical probes P_2 and

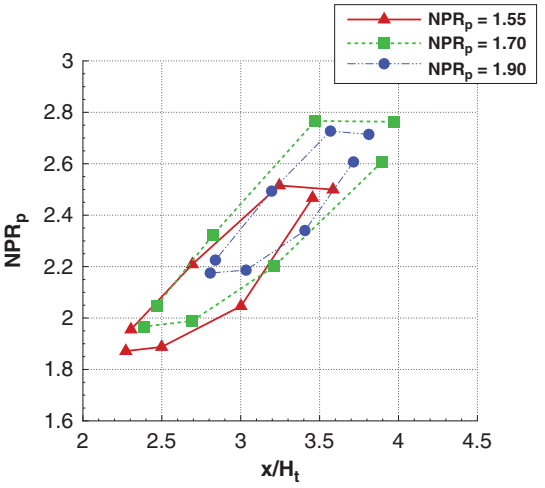

Fig. 13 Hysteresis cycle of the local nozzle pressure ratio NPR$_p$ for all the nominal NPRs.

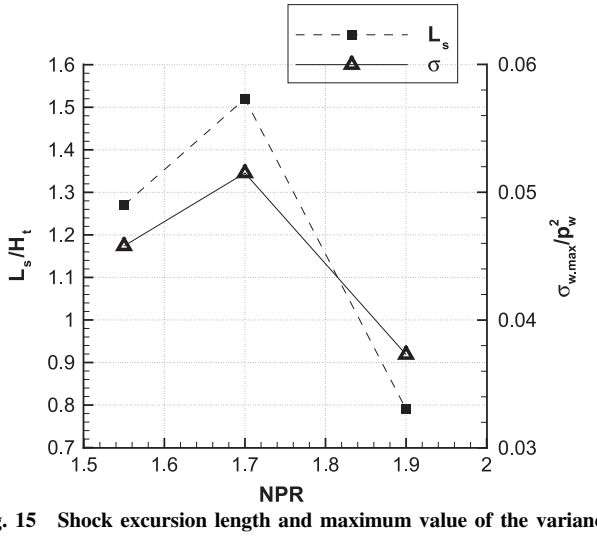

Fig. 15 Shock excursion length and maximum value of the variance along the longitudinal axis.

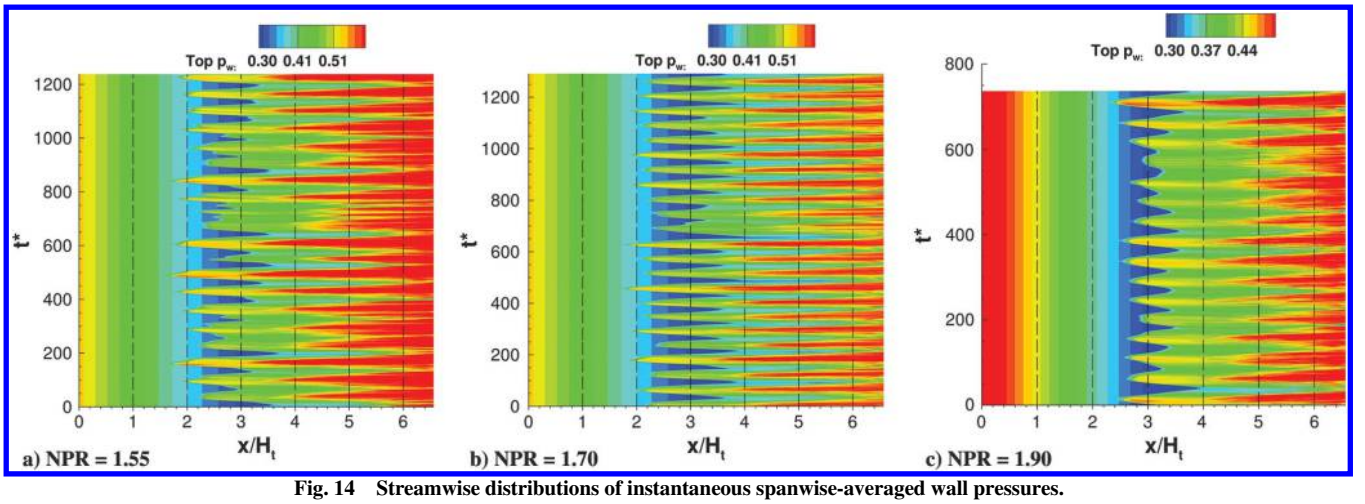

Fig. 14 Streamwise distributions of instantaneous spanwise-averaged wall pressures.

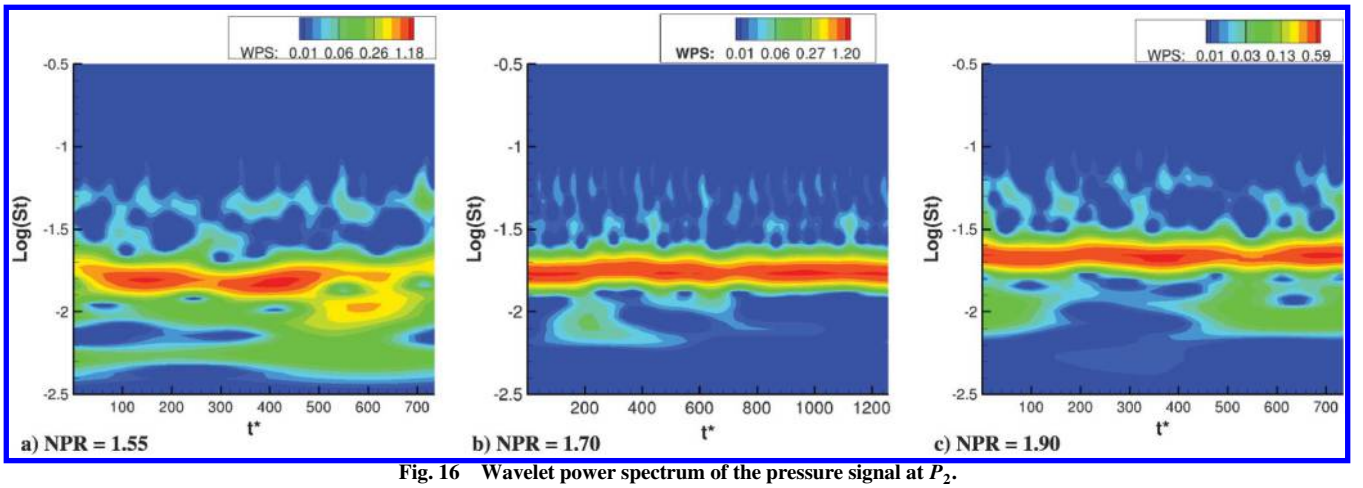

Fig. 16 Wavelet power spectrum of the pressure signal at P_2.

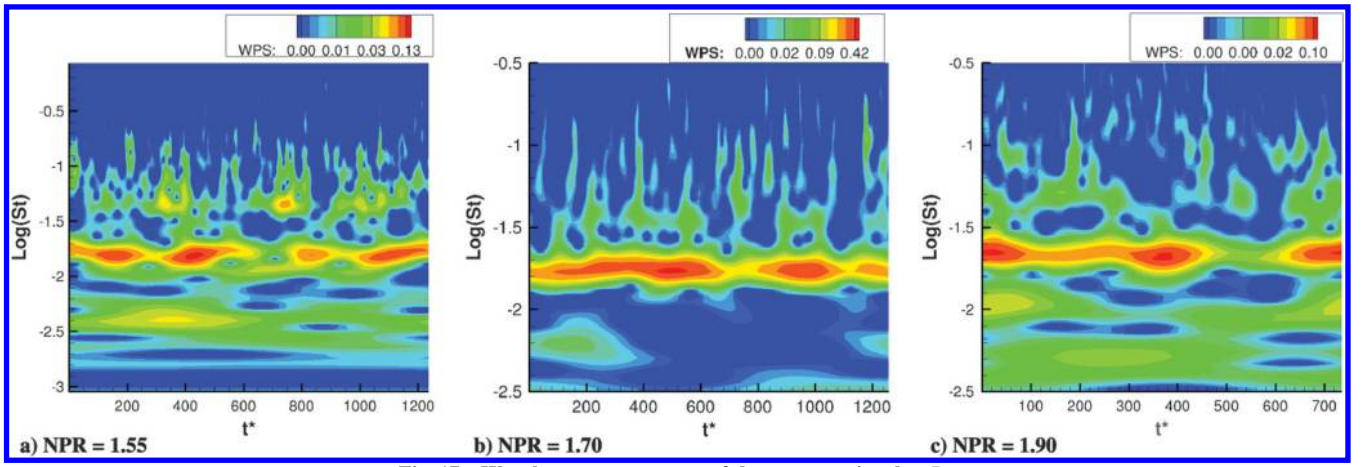

Fig. 17 Wavelet power spectrum of the pressure signal at P_3.

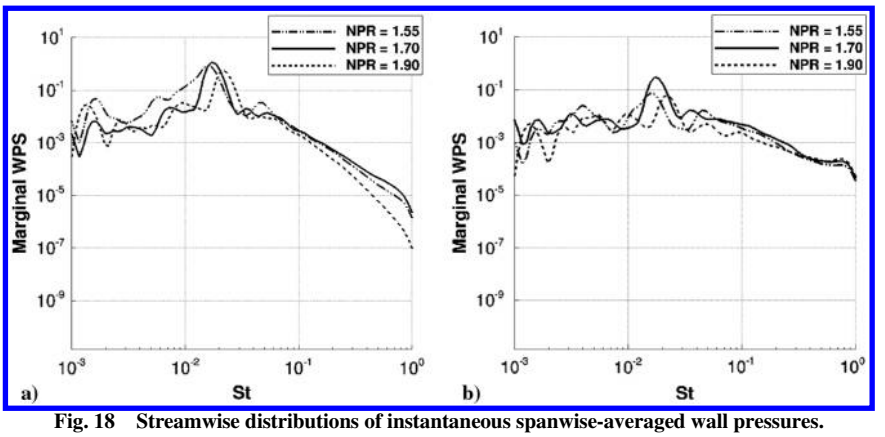

Fig. 18 Streamwise distributions of instantaneous spanwise-averaged wall pressures.

P_3 are analyzed. Figure 16 shows the WPS for the signals from P_2. In all the cases, the dominant contribution from the shock movement can be seen, but at NPR = 1.55, this prevalent mode is more influenced by the turbulence intermittency, and in fact it alternates zones of high energy with zones of low energy. Figure 17 shows the wavelet power spectrum for probe P_3. Although at NPR = 1.70 there is an important trace of the shock motion at low frequencies, this trace is reduced at NPR = 1.55 and 1.90. The shock motion appears as energetic spots with a frequency and amplitude modulation. The characteristics of the turbulent region appear as spots at higher frequencies, and they are very similar for all the NPRs.

Figure 18 compares the marginal wavelet power spectrum for the three cases at probe P_2 and P_3. It can be seen that, on average, NPR = 1.70 is the case characterized by the higher energy in the pressure fluctuations, both in the shock region and in the turbulent separated region. The peaks in the marginal spectrum allow us also to identify the most probable shock Strouhal numbers, which are reported in Table 2. The shock Strouhal number increases with the

Table 2 Shock Strouhal numbers of the simulated NPRs

NPR	St
1.55	0.0158
1.70	0.0172
1.90	0.0223

shock strength, as also was found numerically in Olson and Lele [16] and experimentally in Johonson and Papamoschou [8].

VI. Conclusions

A delayed detached-eddy simulation of a planar nozzle with flow separation has been carried out, and the results have been compared with experimental and LES data taken from literature. The nozzle flow simulated in this study is characterized by a strong nonsymmetric separation shock with a classical lambda shape and by an important recirculation zone. The simulation is able to capture a self-sustained unsteadiness of the shock system. A statistical description of this unsteadiness has been carried out. The shock region and the turbulent separated region are characterized by well-defined peaks in the wall pressure fluctuations standard deviation distribution. This behavior is similar to other canonical SWBLIs, like impinging shocks and compression ramps. The spectral analysis has been carried out using the Morlet wavelet transform, which is a well-suited tool to analyze nonstationary time series. According to the wavelet decomposition, the shock movement is characterized by a concentration of energy around a Strouhal number equal to 0.017. The peak Strouhal number is very close to the reference LES and experimental values. The wavelet power spectrum in the recirculating region is always influenced by the shock movement at $St = 0.017$, but it also shows the effect of the fully development of turbulence. In fact, for Strouhal number greater than the shock Strouhal number, the spectrum is characterized by a collection of alternating high- and low-energy events. The excursion length of the shock is close to the reference LES result, and both are greater than the experimental value. This fact raises a question on the use of periodic boundary conditions in the spanwise direction instead of the real side walls. The shock movement is characterized by a limit-cycle instability, driven by a pressure imbalance of the static pressure behind the shock inside the nozzle with the imposed ambient pressure. The fundamental frequency found in this work is lower than the one foreseen by the analytical model of the acoustical longitudinal resonance (one-quarter wavelength model). It can be argued that an important interplay with the turbulent separated region is present, even if it is still not clear how it could be quantified. A parametric analysis has been conducted varying the nozzle pressure ratio. The major finding is that, at the highest simulated NPR, the shock system is characterized by the constant presence of a large region of reversed flow. For this case, the shock Strouhal number is increased, and the excursion length has an important decrease. The comparison of the wavelet power spectra shows that, at $NPR = 1.70$, the shock movement has the greatest energy and the greatest influence over all the pressure signals.

Acknowledgments

M. Bernardini was supported by the Scientific Independence of Young Researchers program 2014 (Active Control of Shock-Wave/Boundary-Layer Interactions project, grant RBSI14TKWU), which is funded by the Ministero Istruzione Università e Ricerca. The simulations have been performed thanks to computational resources provided by the Cineca Italian Computing Center under the Italian Super Computing Resource Allocation initiative (grant ISCRA C/DESROCK, ISCRA C/DDESNOZ, ISCRA B/DLESRN17). Wavelet software was provided by C. Torrence and G. Compo. The authors also thank Giacomo della Posta, who carried out a part of the data postprocessing.

References

[1] Nave, L., and Coffey, G., "Sea Level Side Loads in High-Area-Ratio Rocket Engines," *9th Propulsion Conference*, AIAA Paper 1973-1284, 1973.

[2] Hadjadj, A., and Onofri, M., "Nozzle Flow Separation," *Shock Waves*, Vol. 19, No. 3, 2009, pp. 163–169. doi:10.1007/s00193-009-0209-7

[3] Reijasse, P., Palerm, S., and Pouffary, B., "Side Loads and Thermal Loads in Rocket Nozzles. Overview of the CNES-ONERA ATAC Programme," *International Journal of Engineering Systems Modelling and Simulation*, Vol. 3, Nos. 1–2, 2011, pp. 87–98. doi:10.1504/IJESMS.2011.038753

[4] Bogar, T. J., Sajben, M., and Kroutil, J. C., "Characteristic Frequency and Length Scales in Transonic Diffuser Flow Oscillations," *AIAA 14th Fluid and Plasma Dynamics Conference*, AIAA Paper 1981-1291, 1981.

[5] Bourgoing, A., and Reijasse, P., "Experimental Analysis of Unsteady Separated Flows in a Supersonic Planar Nozzle," *Shock Waves*, Vol. 14, No. 4, 2005, pp. 251–258. doi:10.1007/s00193-005-0269-2

[6] Handa, T., Masuda, M., and Matsuo, K., "Mechanism of Shock Wave Oscillation in Transonic Diffusers," *AIAA Journal*, Vol. 41, No. 1, 2003, pp. 64–70. doi:10.2514/2.1914

[7] Papamoschou, D., and Zill, A., "Fundamental Investigation of Supersonic Nozzle Flow Separation," *42nd Aerospace Sciences Meeting and Exhibit*, AIAA Paper 2004-1111, Jan. 2004.

[8] Johnson, A., and Papamoschou, D., "Instability of Shock-Induced Nozzle Flow Separation," *Physics of Fluids*, Vol. 22, No. 1, 2010, Paper 016102. doi:10.1063/1.3278523

[9] Verma, S., Chidambaranathan, M., and Hadjadj, A., "Analysis of Shock Unsteadiness in a Supersonic Over-Expanded Planar Nozzle," *European Journal of Mechanics/B Fluids*, Vol. 68, March 2018, pp. 55–65. doi:10.1016/j.euromechflu.2017.11.005

[10] Garnier, E., Sagaut, P., and Deville, M., "Large-Eddy Simulation of Shock/Boundary-Layer Interaction," *AIAA Journal*, Vol. 40, No. 10, 2002, pp. 1935–1944. doi:10.2514/2.1552

[11] Touber, E., and Sandham, N. D., "Large–Eddy Simulation of Low-Frequency Unsteadiness in a Turbulent Shock-Induced Separation Bubble," *Theoretical and Computational Fluid Dynamics*, Vol. 23, No. 2, 2009, pp. 79–107. doi:10.1007/s00162-009-0103-z

[12] Touber, E., and Sandham, N. D., "Low-Order Stochastic Modelling of Low-Frequency Motions in Reflected Shock-Wave/Boundary-Layer Interactions," *Journal of Fluid Mechanics*, Vol. 671, March 2011, pp. 417–465. doi:10.1017/S0022112010005811

[13] Hadjadj, A., "Large-Eddy Simulation of Shock/Boundary-Layer Interaction," *AIAA Journal*, Vol. 50, No. 12, 2012, pp. 2919–2927. doi:10.2514/1.J051786

[14] Aubard, G., Gloerfelt, X., and Robinet, J., "Large-Eddy Simulation of Broadband Unsteadiness in a Shock/Boundary-Layer Interaction," *AIAA Journal*, Vol. 51, No. 10, 2013, pp. 2395–2409. doi:10.2514/1.J052249

[15] Deck, S., "Delayed Detached Eddy Simulation of the End-Effect Regime and Side-Loads in an Overexpanded Nozzle Flow," *Shock Waves*, Vol. 19, No. 3, 2009, pp. 239–249. doi:10.1007/s00193-009-0199-5

[16] Olson, B. J., and Lele, S. K., "A Mechanism for Unsteady Separation in Over-Expanded Nozzle Flow," *Physics of Fluids*, Vol. 25, No. 11, 2013, Paper 110809. doi:10.1063/1.4819349

[17] Spalart, P., Jou, W., Strelets, M., and Allmaras, S., "Comments on the Feasibility of LES for Wings, and on a Hybrid RANS/LES Approach," *Advances in DNS/LES*, edited by C. Liu, and Z. LiuGreyden Press, Columbus, OH, 1997, pp. 137–147.

[18] Martelli, E., Ciottoli, P. P., Bernardini, M., Nasuti, F., and Valorani, M., "Detached Eddy Simulation of Shock Unsteadiness in an Over-Expanded Planar Nozzle," *AIAA Journal*, Vol. 55, No. 6, 2017, pp. 2016–2028. doi:10.2514/1.J055273

[19] Shur, M. L., Spalart, P. R., Strelets, M. K., and Travin, A. K., "An Enhanced Version of DES with Rapid Transition from RANS to LES in Separated Flows," *Flow, Turbulence and Combustion*, Vol. 95, No. 4, 2015, pp. 709–737. doi:10.1007/s10494-015-9618-0

[20] Torrence, C., and Compo, G. P., "A Practical Guide to Wavelet Analysis," *Bulletin of the American Meteorological Society*, Vol. 79, No. 1, 1998, pp. 61–78. doi:10.1175/1520-0477(1998)079<0061:APGTWA>2.0.CO;2

[21] Spalart, P. R., "Detached-Eddy Simulation," *Annual Review of Fluid Mechanics*, Vol. 41, 2009, pp. 181–202. doi:10.1146/annurev.fluid.010908.165130

[22] Spalart, P., Deck, S., Shur, M., Squires, K., Strelets, M., and Travin, A., "A New Version of Detached-Eddy Simulation, Resistant to Ambiguous Grid Densities," *Theoretical and Computational Fluid Dynamics*,

Vol. 20, No. 3, 2006, pp. 181–195.
doi:10.1007/s00162-006-0015-0

[23] Deck, S., "Recent Improvements in the Zonal Detached Eddy Simulation (ZDES) Formulation," *Theoretical and Computational Fluid Dynamics*, Vol. 26, No. 6, 2012, pp. 523–550.
doi:10.1007/s00162-011-0240-z

[24] Memmolo, A., Bernardini, M., and Pirozzoli, S., "Scrutiny of Buffet Mechanisms in Transonic Flow," *International Journal for Numerical Methods Heat Fluid Flow*, Vol. 28, No. 5, 2018, pp. 1031–1046.

[25] Jameson, A., "Formulation of Kinetic Energy Preserving Conservative Schemes for Gas Dynamics and Direct Numerical Simulation of One-Dimensional Viscous Compressible Flow in a Shock Tube Using Entropy and Kinetic Energy Preserving Schemes," *Journal of Scientific Computing*, Vol. 34, No. 2, 2008, pp. 188–208.
doi:10.1007/s10915-007-9172-6

[26] Pirozzoli, S., "Numerical Methods for High-Speed Flows," *Annual Review of Fluid Mechanics*, Vol. 43, 2011, pp. 163–194.
doi:10.1146/annurev-fluid-122109-160718

[27] Ducros, F., Ferrand, V., Nicoud, F., Darracq, D., Gacherieu, C., and Poinsot, T., "Large-Eddy Simulation of the Shock/Turbulence Interaction," *Journal of Computational Physics*, Vol. 152, No. 2, 1999, pp. 517–549.
doi:10.1006/jcph.1999.6238

[28] Bernardini, M., and Pirozzoli, S., "A General Strategy for the Optimization of Runge–Kutta Schemes for Wave Propagation Phenomena," *Journal of Computational Physics*, Vol. 228, No. 11, 2009, pp. 4182–4199.
doi:10.1016/j.jcp.2009.02.032

[29] Driscoll, T. A., and Vavasis, S. A., "Numerical Conformal Mapping Using Cross-Ratios and Delaunay Triangulation," *SIAM Journal on Scientific Computing*, Vol. 19, No. 6, 1998, pp. 1783–1803.
doi:10.1137/S1064827596298580

[30] Olson, B., and Lele, S., "Large-Eddy Simulation of an Over-Expanded Planar Nozzle," *41st AIAA Fluid Dynamics Conference and Exhibit*, AIAA Paper 2011-3908, June 2011.

[31] Pirozzoli, S., Bernardini, M., and Grasso, F., "Characterization of Coherent Vortical Structures in a Supersonic Turbulent Boundary Layer," *Journal of Fluid Mechanics*, Vol. 613, Oct. 2008, pp. 205–231.
doi:10.1017/S0022112008003005

[32] Östlund, J., "Flow Process in Rocket Engine Nozzles with Focus on Flow Separation and Side-Loads," Ph.D. Thesis, Royal Inst. of Technology, Stockholm, 2002.

[33] Martelli, E., Nasuti, F., and Onofri, M., "Numerical Calculation of FSS/RSS Transition in Highly Overexpanded Rocket Nozzle Flows," *Shock Waves*, Vol. 20, No. 2, 2010, pp. 139–146.
doi:10.1007/s00193-009-0244-4

[34] Matsuo, K., Miyazato, Y., and Kim, H.-D., "Shock Train and Pseudo-Shock Phenomena in Internal Gas Flows," *Progress in Aerospace Sciences*, Vol. 35, No. 1, 1999, pp. 33–100.
doi:10.1016/S0376-0421(98)00011-6

[35] Xiong, B., Fan, X.-Q., Wang, Z.-G., and Tao, Y., "Analysis and Modelling of Unsteady Shock Train Motions," *Journal of Fluid Mechanics*, Vol. 846, July 2018, pp. 240–262.
doi:10.1017/jfm.2018.209

[36] Dupont, P., Haddad, C., and Debiève, J. F., "Space and Time Organization in a Shock-Induced Separated Boundary Layer," *Journal of Fluid Mechanics*, Vol. 559, July 2006, p. 255.
doi:10.1017/S0022112006000267

[37] Pirozzoli, S., and Bernardini, M., "Direct Numerical Simulation Database for Impinging Shock Wave/Turbulent Boundary-Layer Interaction," *AIAA Journal*, Vol. 49, No. 6, 2011, pp. 1307–1312.
doi:10.2514/1.J050901

[38] Dolling, D. S., and Or, C. T., "Unsteadiness of the Shock Wave Structure in Attached and Separated Compression Ramp Flows," *Experiments in Fluids*, Vol. 3, No. 1, 1985, pp. 24–32.
doi:10.1007/BF00285267

[39] Farge, M., "Wavelet Transforms and Their Applications to Turbulence," *Annual Review of Fluid Mechanics*, Vol. 24, 1992, pp. 395–458.
doi:10.1146/annurev.fl.24.010192.002143

[40] Zaman, K. B. M. Q., Dahl, M. D., Bencic, T. J., and Loh, C. Y., "Investigation of a 'Transonic Resonance' with Convergent Divergent Nozzles," *Journal of Fluid Mechanics*, Vol. 463, July 2002, pp. 313–343.
doi:10.1017/S0022112002008819

[41] Morse, P., *Vibration and Sound*, McGraw–Hill, New York, 1948.

J. Poggie
Associate Editor